ADVANCED FUNCTIONAL MATERIALS
www.afm-journal.de

Trap-Assisted Transport and Neuromorphic Plasticity in Lead-Free 2D Perovskites PEA_2SnI_4

Ofelia Durante, Valeria Demontis, Jonas Riisnaes Karl, Lam Hoi Tung, Sebastiano De Stefano, Daniela Marongiu, Adolfo Mazzotti, Aditya Bhardwaj, Francesco Mattana, Elisa Pili, Selene Matta, Federico Paolucci, Michele Saba, Andrea Mura, Giovanni Bongiovanni, Monica F Craciun, Saverio Russo,* and Antonio Di Bartolomeo**

Tin-based perovskites offer one of the most viable sustainable alternatives to their lead counterparts, combining comparable band structures with strong visible-light absorption and favorable charge transport. Most studies have focused on thin films, where grain boundaries dominate charge transport, and the large surface area accelerates the oxidation of tin, obscuring the intrinsic properties of the material. Here, single crystals of phenethylammonium tin iodide (PEA_2SnI_4) are investigated, isolating their fundamental optoelectronic response from film-related artefacts. It is found that air and light exposure primarily affect surface layers, with partial recovery achievable through exfoliation. Photodetectors fabricated from single crystals exhibit a photoresponsivity of ≈60 A W^{-1} under low-intensity 650 nm illumination, with photocurrent scaling quadratically with bias in a space charge-limited current regime, and transport displaying a transition from thermal excitation to phonon scattering at 225 K. Time-resolved photocurrent measurements further reveal prolonged decay dynamics and cumulative pulse responses, characteristic of short-term synaptic plasticity such as temporal integration and voltage-modulated persistence. These findings establish PEA_2SnI_4 single crystals as a benchmark for understanding degradation and transport in lead-free perovskites, while positioning them as a viable materials platform for neuromorphic vision and adaptive optoelectronics.

1. Introduction

In recent years, metal halide perovskites have emerged as versatile semiconductor materials for a wide range of optoelectronic applications, including solar cells, light-emitting diodes, field-effect transistors and photodetectors.[1–7] Their remarkable optoelectronic properties, such as high absorption coefficients, long carrier scattering lengths and tunable band gaps, make them ideal candidates for high-performance, low-cost device architectures. However, the widespread use of lead-based perovskites, in particular methylammonium lead iodide ($MAPbI_3$),[8] formamidinium lead iodide ($FAPbI_3$),[9] and cesium lead bromide ($CsPbBr_3$),[10,11] has raised concerns due to the inherent toxicity, environmental persistence and potential bioaccumulation of lead.[12–14] These safety and environmental risks have prompted the development of lead-free alternatives that retain the desirable optoelectronic characteristics of their lead-based counterparts

---

O. Durante, S. De Stefano, A. Mazzotti, A. Di Bartolomeo
Department of Physics 'E.R. Caianiello'
University of Salerno
Via Giovanni Paolo II 132, Fisciano, SA 84084, Italy
E-mail: adibartolomeo@unisa.it

V. Demontis, D. Marongiu, A. Bhardwaj, F. Mattana, E. Pili, S. Matta, M. Saba, A. Mura, G. Bongiovanni
Department of Physics
University of Cagliari
Monserrato, CA 09042, Italy
E-mail: vdemontis@dsf.unica.it

The ORCID identification number(s) for the author(s) of this article can be found under https://doi.org/10.1002/adfm.202526339

DOI: 10.1002/adfm.202526339

V. Demontis, F. Paolucci
INFN Sezione di Pisa
Largo Bruno Pontecorvo 3, Pisa I-56127, Italy

J. R. Karl, L. H. Tung, S. Russo
Centre for Graphene Science
Department of Physics
University of Exeter
StockerRoad 6, Exeter EX4 4QL, UK
E-mail: s.russo@exeter.ac.uk

F. Paolucci
Department of Physics 'E. Fermi'
University of Pisa
Largo Pontecorvo 3, Pisa I-56127, Italy

M. F Craciun
Centre for Graphene Science
Department of Engineering
University of Exeter
North Park Road, Exeter EX4 4QF, UK

while offering a more sustainable material platform. Among the candidates explored, tin (Sn)-based perovskites have attracted considerable attention due to their electronic structure and ionic radius similar to that of lead,[15] which allows for comparable structural and optoelectronic behaviour,[16–23] despite the low environmental stability of Sn-based perovskites remaining a critical challenge.[24–27] In particular, hybrid organic/inorganic layered (2D) phenethylammonium tin iodide, PEA_2SnI_4 perovskites offer advantages such as an improved environmental stability compared to 3D tin-based perovskites, due to the presence of the large organic spacers acting as hydrophobic protective layers,[28] enhanced in-plane conductivity, multiple quantum well (MQW) structures, and relatively high hole mobility.[19,29] Furthermore, their compatibility with low-temperature solution processing techniques makes them suitable for integration into flexible and wearable electronics.[30] Notably, PEA_2SnI_4 was also among the first 2D halide perovskites to exhibit p-type field-effect transistor (FET) behaviour, with promising mobility and stability parameters under ambient conditions.[31] Moreover, Sn-based perovskites face critical challenges, such as the tendency for Sn to oxidise from Sn^{2+} to Sn^{4+}, resulting in p-type self-doping, increased defect density and reduced device stability.[17,20,32] However, these ionic properties, often seen as limitations in traditional semiconductors, can instead be exploited as active mechanisms in emerging device paradigms. The rapid ion migration and defect-mediated dynamics intrinsic to hybrid perovskites have recently been exploited to design reconfigurable memory devices, light-controlled logic elements, and optoelectronic synapses that can mimic biological learning.[33–36] In this context, hybrid organic/inorganic layered perovskites have emerged as a particularly attractive class of materials. In these 2D systems, charges are confined in the inorganic metal-halide octahedral layers, which are separated by bulky organic spacer cations, effectively resulting in self-assembled quantum wells. These 2D materials follow the general formula $(A')_2(A)_{n-1}B_nX_{3n+1}$, where A' is a large organic cation (e.g., phenethylammonium), A is a small monovalent cation (e.g., methylammonium), B is a divalent metal (e.g., Sn^{2+}), X is a halide anion and n is the number of octahedral layers enclosed between planes of organic cations. The incorporation of large hydrophobic organic cations reduces the structural dimensionality, transitioning from a 3D ($n = \infty$) to a 2D ($n = 1$) architecture, and enhances moisture resistance while maintaining efficient charge transport within the inorganic layers.[17,37,38] Most practical devices are presently based on polycrystalline thin films, which are realised by relatively simple techniques such as spin coating, blade coating, evaporation, etc. Polycrystalline perovskites inherently possess a more complex morphology, including grain boundaries, disordered domains, and surface inhomogeneities.[39–41] These defects often act as recombination centres, trap states, and ion migration channels, significantly impacting device performance. However, achieving high-quality monocrystalline thin films remains a significant challenge. Whilst single-crystal halide perovskites have historically been grown as bulk single crystals,[42] the synthesis of single-crystal thin films with controlled thickness and large-area uniformity remains an open challenge.[43]

In this work, we present a systematic study of the optoelectronic response and charge transport dynamics of single-crystal thin films, PEA_2SnI_4-based photodetectors fabricated on large-area interdigitated electrodes. We demonstrate a maximum photoresponsivity of ≈60 A W^{-1} under low-intensity 650 nm illumination. Analysis of the dependence on light power and voltage bias confirms that the devices operate in a trap-assisted space-charge-limited current (SCLC) regime. The SCLC transport frequently dominates in semiconductors such as organic semiconductors and hybrid perovskites with low intrinsic carrier concentrations, where carrier injection from contacts exceeds thermally generated carriers, leading to an electrical response dominated by the bulk properties of the material and the presence of trap states.[44,45] SCLC results in unique dark current–voltage (J–V) characteristics governed by defect-mediated transport, trap filling, and carrier accumulation dynamics under applied electric fields.[46,47] Time-resolved photocurrent measurements reveal a slow, voltage-dependent decay characteristic of trap-mediated dynamics, while temperature-dependent transport shows a clear crossover ≈225 K from thermally activated conduction to a phonon-limited regime. Importantly, the persistent photocurrent and cumulative pulse responses observed mimic key features of biological short-term synaptic plasticity, opening pathways toward neuromorphic vision applications based on lead-free, environmentally friendly perovskites.

2. Synthesis, Morphology, and Optical Characterization of PEA_2SnI_4 Single Crystals

Single-crystal PEA_2SnI_4 thin films were grown using the space-confined approach on 1.5 cm × 1.5 cm quartz substrates, cleaned and thermalized according to growth protocols outlined in previous works.[1] **Figure 1a** shows an optical image of a representative crystal under white light (main panel) and UV illumination (inset). The intense red photoluminescence (PL) of PEA_2SnI_4 observed under ultraviolet excitation is well documented, especially for polycrystalline thin films,[26,48] and is attributed to band-edge excitonic recombination. The crystals typically grow in a ribbon-like morphology, similar to their lead-based counterparts,[1] with thicknesses of ≈600 nm or less, lengths extending to the centimeter scale, and widths of several hundred micrometers. Figure 1b presents a scanning electron microscopy (SEM) image of a smaller crystal, confirming the ribbon-shaped geometry with well-defined edges and smooth surface features, consistent with a preferential in-plane growth direction. Figure 1c shows an atomic force microscopy (AFM) image of a part of the large ribbon-shaped single crystal, measured on a scan area of 5.4 µm × 4.2 µm. The AFM image reveals terraces on the surface of the crystal, typical of layered 2D perovskites, with heights corresponding to multiples of the thickness of the perovskite single layers.[49,50] The Root-Mean-Square (RMS) roughness of 2.5 nm measured on the terrace suggests a flat and uniform surface, which is favourable for the subsequent integration of optoelectronic devices, as it promotes good interfacial contact and minimises scattering or loss of carriers through layered structures. Figure 1d shows the absorption spectrum (left axis) and the photoluminescence (PL) spectrum (right axis) under 395 nm excitation, both measured at room temperature on a freshly prepared sample. The optical absorption spectrum is characterized by an evident excitonic peak, centred around 610 nm, corresponding to an energy value of 2.03 eV. The PL spectrum shows a prominent emission peak located at ≈635 nm, in agreement with

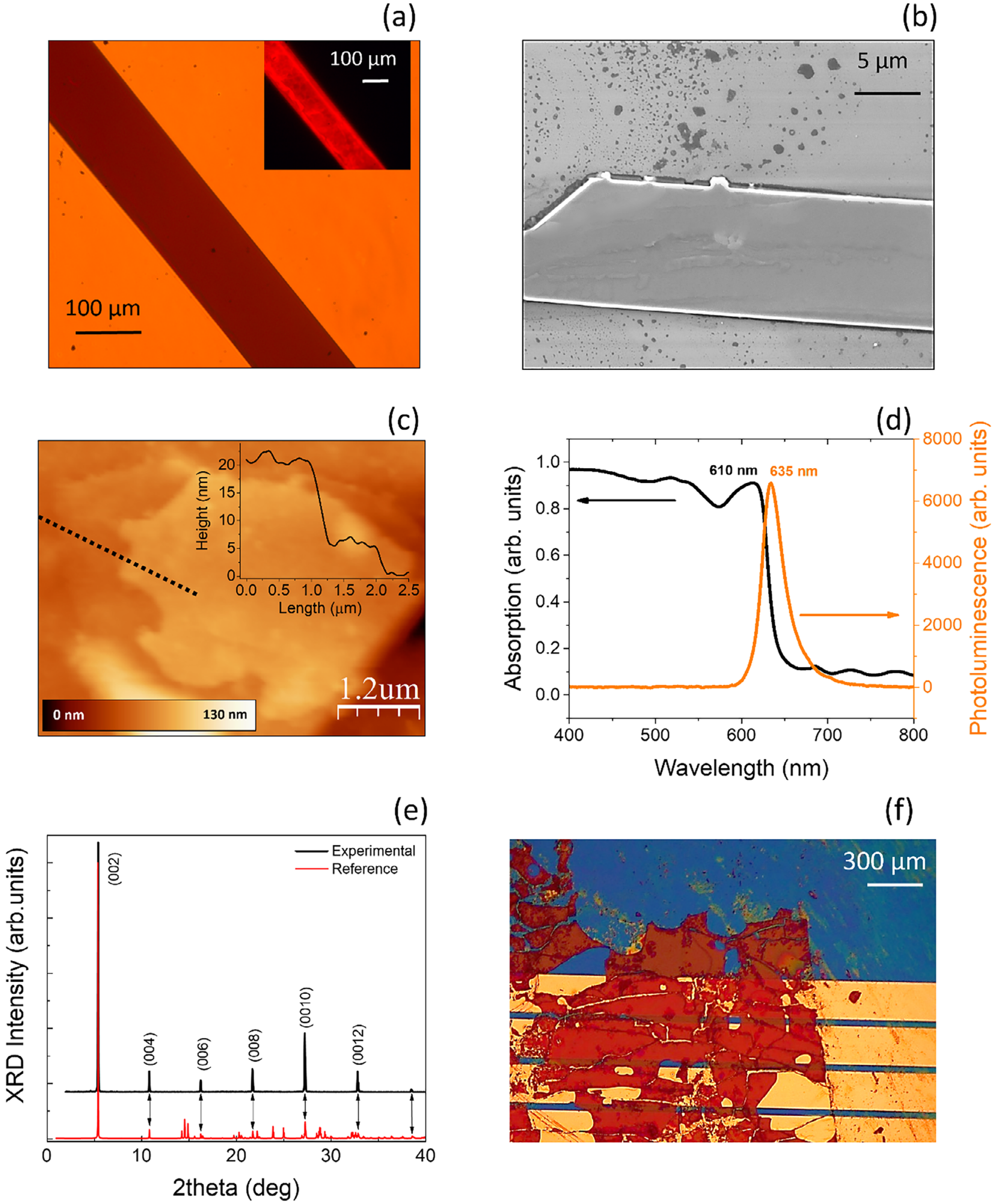

Figure 1. a) Optical image of the as-grown samples at 50× magnification. Inset: optical image under UV illumination, displaying luminescence in the red. b) SEM and c) AFM images of the crystal surface. Inset: AFM profile. d) Photoluminescence (PL) (under 395 nm excitation) and absorption spectra were measured at room temperature. e) XRD pattern of $(PEA)_2SnI_4$ single crystals (black) and reference spectrum (red) extracted from the CIF file for PEA_2SnI_4 from the crystallographic database (COD:4001467). f) Optical image of the $(PEA)_2SnI_4$ interdigitated device.

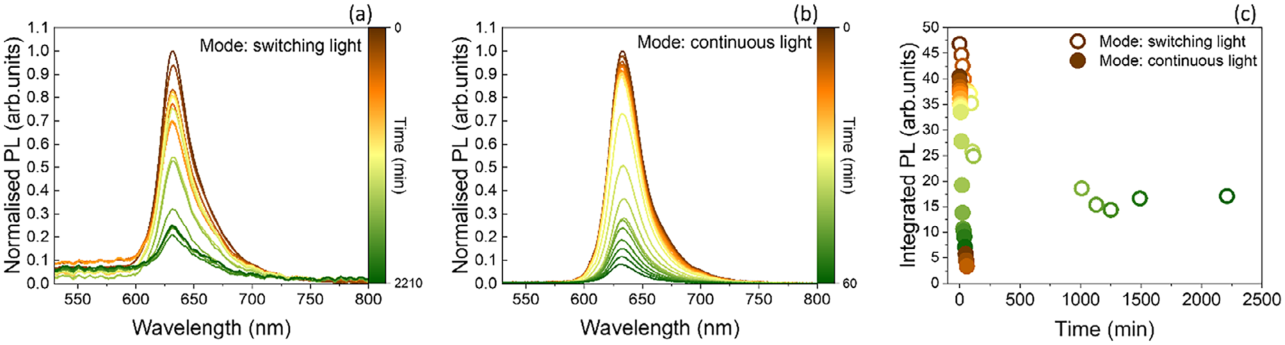

Figure 2. a) Time evolution of the normalised photoluminescence (PL) spectra of PEA_2SnI_4 acquired under excitation at 405 nm in ambient air. Each spectrum was measured at the indicated time while the sample was kept in the dark between acquisitions. b) Normalised PL spectra of the same sample acquired at the indicated time while the sample was kept under continuous illumination at 405 nm and in ambient air. c) Comparison of decay curves of the integrated PL intensity when the sample is kept in the dark between acquisition (dark squares) and when it is kept under constant light irradiation (orange squares).

previous reports.[51] The spectral difference in the position of the band maximum of the emission and absorption, known as Stokes shift (ΔE_s), is a well-reported phenomenon in hybrid perovskites. It arises in part because absorption is an instantaneous mechanism involving different excited states, whereas photoluminescence (PL) emission results from interband electronic transitions after lattice relaxation.[52] In addition, the large film thickness leads to significant self-absorption of the emitted light, which further contributes to the observed shift. Figure 1e shows the X-ray Diffraction (XRD) (black line) compared with the simulated powder diffractogram calculated from the CIF file for PEA_2SnI_4 from the crystallographic database (COD:4001467) (red line). The experimental pattern displays a series of regularly spaced diffraction peaks, indexed as (002), (004), (006), (008), (0010) and (0012), whose 2θ positions coincide with those of the reference pattern, confirming the formation of the targeted PEA_2SnI_4 phase. The exclusive presence of (00l) peaks and the strong enhancement of the (002) reflection indicate a highly oriented crystal with the perovskite layers parallel to the substrate (c-axis out of plane), and the absence of additional peaks attests to the high crystallinity and phase purity of the sample.

Finally, the single crystal flakes were mechanically transferred onto a gold interdigitated pattern, with 7 µm spacing, fabricated on a Si^{++}/SiO_2 (280 µm, 300 nm) substrate, as shown in Figure 1f.

3. Results and Discussion

3.1. Stability of PEA_2SnI_4 Single Crystals

First, we assessed the environmental stability of PEA_2SnI_4 material by monitoring its photoluminescence (PL) intensity during exposure to ambient air. **Figure** 2a shows the time evolution of PL spectra acquired at regular time intervals (intermittent illumination) using an LED with excitation wavelength $\lambda = 405$ nm (power 1 mW), while the sample was kept in the dark between measurements. The PL spectra show a progressive decrease in intensity over time, accompanied by a broadening of the emission peak compatible with an increasing contribution of sub-gap defect states. To further assess the impact of continuous illumination on stability, a second series of measurements was conducted on a second crystal grown on the same substrate, this time exposing the sample to continuous illumination with the same light source ($\lambda = 405$ nm at 1 mW) for the entire duration of the PL measurement sequence (Figure 2b).

The integrated PL intensity as a function of time is reported in Figure 2c. For the sample measured under intermittent illumination (dark squares), the PL intensity shows a marked decrease during the first hour of exposure to the environment. This rapid initial decay is attributed to the degradation of the outermost layers of the perovskite film, which are particularly sensitive to oxygen and moisture.[24–26] In tin-based perovskites, the oxidation of Sn^{2+} to Sn^{4+} is a well-documented degradation pathway that leads to the formation of deep defects and non-radiative recombination centers, which rapidly quench the radiative emission of the material.[27] The PL signal partially stabilizes over longer periods (up to 2200 min), suggesting that the bulk of the material remains relatively unaffected once the surface has oxidized, forming a passivating layer. Under continuous illumination (orange squares in Figure 2c), degradation proceeds much more rapidly, with almost complete quenching of the integrated PL within an hour. This accelerated degradation under light confirms the presence of a photoinduced degradation mechanism, probably related to the combined action of light, oxygen and residual moisture, which favors the formation of mobile halide vacancies and irreversible structural damage.[38]

These results reveal that the instability of pristine PEA_2SnI_4 under ambient conditions, in particular under continuous illumination, is mostly related to surface degradation. We observed that the PL signal could be fully recovered after exfoliation of the upper surface layers using an adhesive tape (Nitto), confirming that degradation is predominantly a process limited to the surface, while the crystal bulk retains the optical properties for several months. Figure S1 (Supporting Information) presents a comparison between the PL spectrum of the degraded sample and that of the same sample after removal of the upper surface layers (Figure S1c, Supporting Information). The comparison of the optical images of the sample before and after exfoliation is also shown in Figure S1a,b (Supporting Information). The AFM image further confirms the high crystalline quality of the sample, revealing a well-defined layered structure (Figure S1d, Supporting Information). These findings are consistent with recent

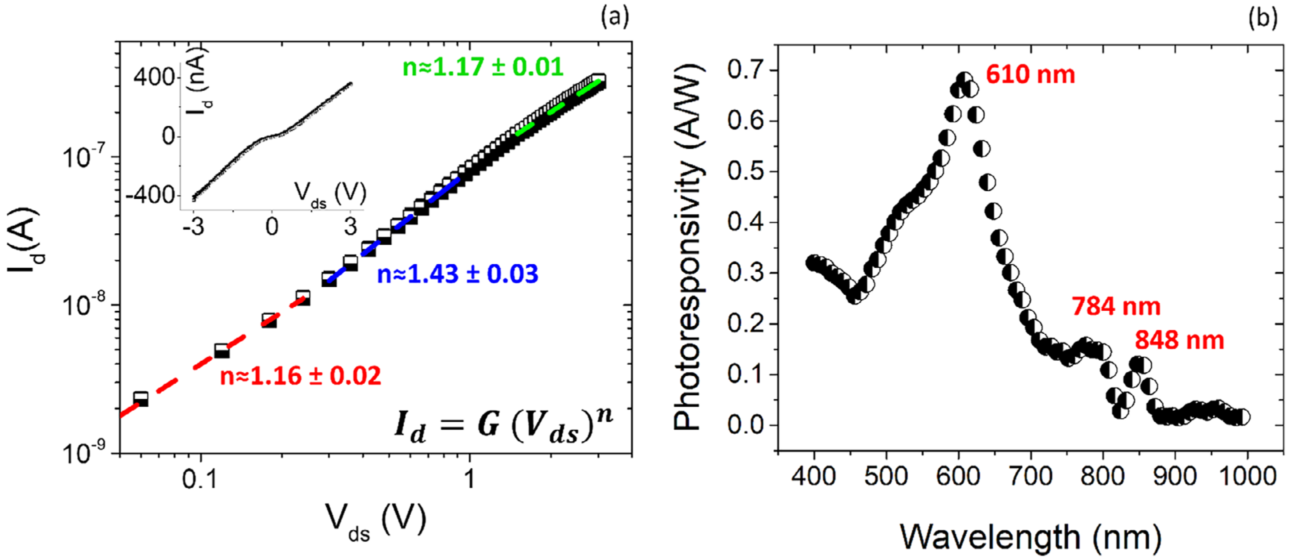

Figure 3. a) Log–log dark *I*–*V* of PEA_2SnI_4 device. An almost linear regime (slope = 1.16 ± 0.02) below 0.25 V evolves into a superlinear trap-limited SCLC regime above 0.3 V with a slope of 1.43 ± 0.03. The restoration of the linear regime is observed above 1.5 V. Inset: dark current-voltage characteristics plotted on a linear scale. b) Photoresponsivity at $V_{bias} = 3$ V. The measurements are performed at a pressure of 10^{-5} mbar.

simulation studies, which indicate that tin oxidation is energetically unfavorable in the bulk of tin-based perovskites but becomes significantly more favorable at unpassivated surfaces.[53] When kept in a vacuum, the sample remains stable for at least two weeks, ensuring stability throughout the entire duration of the experiment (Figure S1e, Supporting information).

The observation that degradation is not intrinsic, but proceeds from the surface, suggests that future stabilization strategies, such as surface passivation, encapsulation or interface engineering, could effectively preserve the properties of this perovskite, enabling its exploitation in optoelectronic and neuromorphic technologies.

These findings were confirmed by the study of the temporal evolution of the dark IV characteristics upon air exposure and in a vacuum. The results are presented in the Supporting Information (see Figure S2, Supporting Information), where we show that the decay of the dark IV upon air exposure (Figure S2a, Supporting Information) displays a similar behavior with respect to the photoluminescence decay, while the device is stable in vacuum (Figure S2b, Supporting Information).

3.2. Photoconductivity of PEA_2SnI_4 Single Crystals

The electrical photoresponse of the PEA_2SnI_4 single crystal-based devices was initially investigated at room temperature and at a pressure of 10^{-5} mbar to prevent degradation of the material by moisture and other atmospheric species. **Figure 3a** presents the dark current–voltage (*I*–*V*) characteristics plotted on a log–log scale, with a linear scale shown in the inset. At low bias ($|V_{ds}| < 0.25$ V), a quasi-ohmic regime is observed, characterized by a power law of 1.16 ± 0.02, indicative of limited charge injection and negligible space-charge effects. For $0.3\text{V}<V_{ds}<1$ V, the drain current displays a superlinear dependence on V_{ds} with a log-log slope of 1.43 ± 0.03, consistent with trap-limited SCLC transport, in which the density of injected carriers exceeds that of thermally generated free carriers, as expected when the applied bias surpasses the SCLC threshold voltage $V_T = \frac{2qn_0L^2}{\varepsilon}$[54]; using our device geometry and the high-low-bias resistivity, the resulting low n_0 makes this condition reasonably satisfied within this bias range. In a trap-limited SCLC regime, conduction occurs primarily through the progressive filling of trap states, leading to the buildup of space charge within the semiconductor. The relatively high dark current levels support the presence of a significant density of shallow traps, which contribute to the background conductivity, in agreement with previous reports for Sn-based 2D perovskites.[5,55–58] As voltage increases further, trap states become saturated, and the quasi-ohmic regime is restored.

Figure 3b shows a plot of the measured spectrally resolved photoresponsivity (R) in the wavelength range from 400 up to 1000 nm, where $R = Iph/(P\,S)$ with the photocurrent given by the difference of the current measured illuminating the sample and that in the dark ($I_{ph} = I_{light} - I_{dark}$), P is the optical power and S is the device photoactive area (≈3×10^4 μm^2). A maximum of R is observed at around $\lambda = 610$ nm, which corresponds to the excitonic absorption peak dominating the PL spectra (see Figure 2a). A priori, this observation is rather surprising. Under resonant excitation at the exciton energy, only cold excitons are injected into the material. Moreover, the exciton binding energy in PEA_2SnI_4 greatly exceeds the thermal energy and the dipole moment of the excitons is primarily oriented in the electrically conductive plane.[52] On this basis, one would not expect a substantial photocurrent. Our results, however, indicate that resonant exciton generation is accompanied by the spontaneous formation of a free-carrier population. Recent studies on halide perovskites[53] and 2D single-crystal perovskites[2,54] suggest that defect-mediated sub-gap states can create an energy-level "ladder" that assists exciton dissociation. These defect states effectively lower the energetic cost of separating the electron–hole pair, reducing the effective exciton binding energy to below the thermal energy and thereby enabling efficient free-carrier generation in perovskite semiconductors.[59]

Additional photoresponsivity peaks are measured at 784 and 848 nm, see Figure 3b. These observations are consistent with the presence of interstitial Sn defects and Sn vacancies, which have been predicted by recent first-principles density functional theory (DFT) studies on PEA_2SnI_4 to introduce electronic states located ≈0.45 and 0.55 eV above the valence band maximum, respectively.[60] These are related to the well-reported instability of tin and the oxidation from Sn^{2+} to Sn^{+4}.[17–20] A more detailed investigation of the PEA_2SnI_4 photoresponse was conducted under 650 nm illumination, by applying dark/light cycles at different illumination powers, ranging from 0.045 to 121.5 μW (**Figure 4a**). This wavelength was selected because preliminary spectral measurements under constant lamp conditions (prior to power correction) showed the largest photocurrent at 650 nm, and it lies within the high-responsivity region close to the bandedge of PEA_2SnI_4, thus providing a representative operating point for detailed photoresponse analysis. At the highest value of light intensity, the device exhibited a photocurrent of 3.55×10^{-8} A. Figure 4b shows the dependence of the photocurrent on the incident light power, which follows a sublinear power-law trend, $I_{ph} \propto P^{\alpha}$, with an exponent $\alpha = 0.33$, as indicated by the black dashed line. In the absence of traps, a linear scaling of the photocurrent ($\alpha \approx 1$) is expected.[61–63] However, the observed sublinear response is consistent with the presence of sub-gap trap states underpinning the accumulation of charges in the semiconducting channel. This distorts the internal electric field, thus limiting further carrier injection, resulting in suppressed photocurrent response. Finally, the photoresponsivity has a monotonic dependence on the illumination power (see inset in Figure 4b), reaching a maximum value of ≈60 A W^{-1} at a power of 0.074 μW. This functional dependence is consistent with the presence of sub-gap trap states that preferentially capture one charge carrier with respect to the other, either electrons or holes. The free carriers remain mobile for extended periods, circulating multiple times under an applied bias before recombining. This recirculation of carriers gives rise to a photoconductive gain, where the number of charges collected per absorbed photon exceeds unity.[3] At higher incident powers, however, the traps gradually saturate, reducing their ability to prolong carrier lifetimes and thus diminishing the gain. In parallel, space-charge effects, arising from the accumulation of photogenerated carriers, further suppress collection efficiency by distorting the internal electric field.

Figure 4c shows the time-resolved measurements of current exposing the device to alternating periods of dark and illumination with 650 nm light of 121.5 μW (pulses) and varying the voltage bias. The photocurrent shows a rapid rise upon illumination and a slow decay after the light is switched off. The prolonged decay observed in time-resolved photocurrent measurements reveals a persistent behavior of photoconductivity, the duration of which increases with the applied bias. Figure 4d shows the dependence of the photocurrent on the applied bias. The photocurrent increases with V_{bias} following a power law (dashed line), with an exponent close to 2. A very similar result, displayed in Figure S3 (Supporting Information), was obtained by repeating the same measurement at much lower light intensity (1.04 μW). Also, in this case, the photocurrent increases with the applied bias with a power law with an exponent close to 2, revealing that the reduction in the light intensity did not affect the transport regime. This quadratic dependence is related to Mott-Gurney's law for SCLC, typically expressed as[23]:

$$J = \frac{9}{8} \varepsilon \mu \frac{V^2}{d^3} \tag{1}$$

where ϵ is the permittivity of the material, μ is the charge carrier mobility, V is the applied bias voltage, and d is the thickness of the material.

While the Mott–Gurney's law is formally derived for unipolar injection in the absence of photogenerated carriers (i.e., dark conditions), the SCLC behaviour can persist under illumination, especially at low light intensities, in the presence of asymmetric transport for electrons and holes, such as due to trap states and/or blocking contacts. This behavior is consistent with previous reports on hybrid perovskites, where photogenerated carriers can induce space charge effects in the presence of traps or slow recombination dynamics and has also been reported in 2D transition metal dichalcogenides.[44,64]

Importantly, under illumination, in our measurements, we observe a quadratic dependence of the photocurrent across the entire applied bias range (Figure 4d), with no evidence of an initial ohmic J ∝ V regime, which typically precedes SCLC at low voltages in dark conditions. This suggests that the density of photogenerated or injected carriers at the applied voltages is already high enough to dominate over the carrier concentration at equilibrium, as described in Ref. [23] In this case, the current is limited by the accumulation of space charge due to the presence of a high density of traps. This behavior is characteristic of SCLC in perovskite[46,47] and aligns with the significant dark current, which further supports the presence of a trap-rich environment. Such a scenario is plausible in lead-free 2D perovskites like PEA_2SnI_4 at room temperature due to the limited stability of the material. These effects may also influence the temporal persistence of the photocurrent.

The rising and decaying parts of the pulses displayed in Figure 4c are well fitted by a double-exponential function (see dashed colored curves in Figure 4c) by using a double-exponential fit

$$\left(I_{ph} = I_0 + a_1 e^{-\frac{t-t_0}{\tau_1}} + a_2 e^{-\frac{t-t_0}{\tau_2}} \right) \tag{2}$$

where a_1 and a_2 can assume positive or negative values depending on the rise or decay region.

In particular, the two characteristic times $\tau_{1,2}$ account for the fast initial transient displayed in Figure 4c (both in rise and decay) and the subsequent much slower evolution. The sharper and higher photocurrent peaks with increasing bias voltages, displayed in Figure 4c, confirm the field-assisted charge extraction, which is consistent with SCLC behavior. Moreover, the prolonged decay observed in time-resolved photocurrent measurements indicates that the system retains memory of the light stimulus on a time scale of tens to hundreds of seconds.[33,65] This bias-dependent persistence is a distinctive feature of the short-term plasticity mechanisms present in biological synapses, where the history of incoming stimuli influences the subsequent

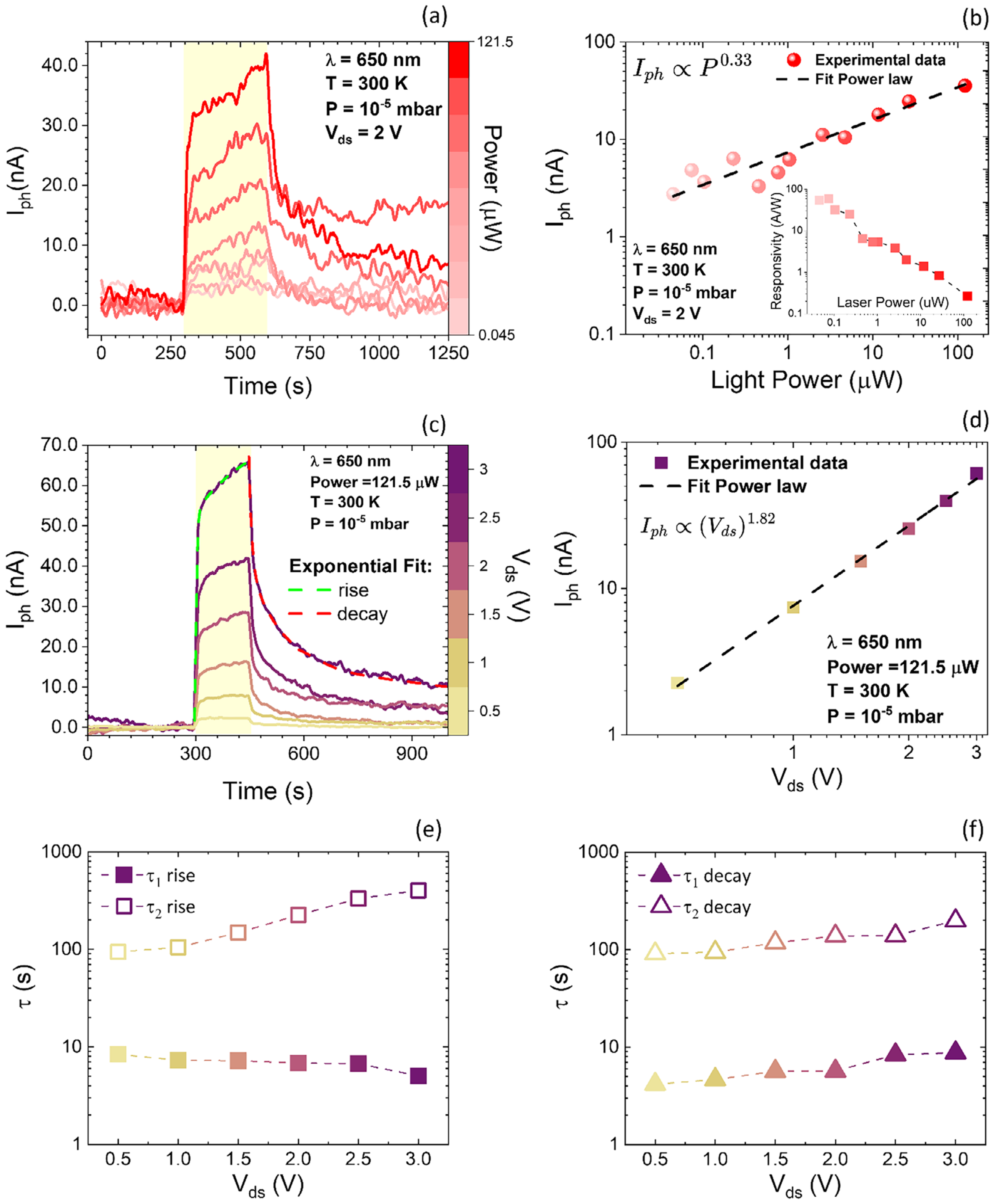

Figure 4. a) Time-resolved photoresponse at different light intensities at a fixed wavelength of 650 nm. b) Photocurrent vs light power on a semi-log scale. c) Photocurrent vs time at different bias voltages at a fixed wavelength of 650 nm and light power of 121.5 μW. d) Photocurrent vs bias voltage at fixed wavelength of 650 nm and light power of 121.5 μW. Extracted relaxation times τ_1 and τ_2 in the (e) rising of the impulse in Figure (c) and the decaying part (f). All measurements are performed at a pressure of 10^{-5} mbar.

synaptic response. In this context, the perovskite-based photodetector behaves similarly to a light-sensitive synaptic element, mimicking essential neuromorphic functionalities such as temporal integration and stimulus-dependent conductance modulation.[66,67] Figure 4e shows the extracted τ_1 and τ_2 for the rise part of the photocurrent at different values of V_{bias}. The two time constants are likely related to two different physical mechanisms. The first characteristic time, τ_1, decreases below the value of 10 s with the increasing V_{bias}, in agreement with previous work on PEA_2SnI_4.[55] The dependence of τ_1 on V_{bias} suggests that this process might be governed by photocarrier extraction from the perovskite material, with the higher electric field accelerating charge separation and drift, thus shortening the response time. The second, longer time constant (τ_2) increases with V_{bias}, indicating a delayed charge collection process likely due to excitation from slower trap states. A similar behaviour is observed in Figure 4f, where the decay dynamics are shown.

The presence of dual exponential components in both the rise and decay phases, with a bias-dependent τ_2, closely resembles the behaviour of artificial synapses exhibiting short-term plasticity.[34–36] In particular, voltage-tunable persistence and temporal asymmetry between the rise and fall dynamics mimic key neuromorphic features such as coupled impulse facilitation, signal integration and volatile memory storage.[33,68] These functionalities are essential for vision-based sensing, adaptive learning systems and optical pre-processing units in neuromorphic circuits.

To further highlight the neuromorphic capabilities of our PEA_2SnI_4 based photodetector, we performed a sequential pulse illumination experiment with increasing bias voltages. As shown in **Figure 5a**, the device exhibits a cumulative photocurrent response, with each optical stimulus producing a step increase with respect to the previous one.[33] In particular, the photocurrent does not return to its baseline between pulses, indicating a slow relaxation process that becomes more pronounced at higher biases. This behavior is a manifestation of stimulus-dependent signal integration, a fundamental characteristic of biological vision systems.[18,33] In our case, the photocurrent plays the role of excitatory post-synaptic current (EPSC), a key element in neural communication and learning. It integrates successive light inputs over time, and the prolonged decay between pulses is reminiscent of transient memory storage in biological synapses. This slow recombination process, regulated by trap filling and ionic redistribution, reflects a plastic system capable of encoding information temporally, rather than simply responding in a binary (on/off) manner. As conceptually illustrated in Figure 5b, which shows a direct analogy with the biological visual processing pathway, the $(PEA)_2SnI_4$ device functions as an artificial retina-synapse interface.

The scheme is structured in four key functional blocks – sensing, transduction, transmission and output – that reflect the operations performed by the human retina-synapse-brain interface. In the detection phase, incoming light is absorbed by the $(PEA)_2SnI_4$ active layer, which functions analogously to the photoreceptive layer of the human retina. This is followed by the transduction stage, in which incident photons generate electron-hole pairs via absorption in the perovskite layer. This process mimics the action of retinal photoreceptor cells that convert light into biochemical signals. Subsequently, in the transmission stage, internal electric fields and the applied bias voltage facilitate charge separation and transport. This is directly analogous to the signal propagation across biological synapses, where neurotransmitters mediate the conversion of input into electrical postsynaptic potentials. In the output stage, the resulting photocurrent represents the device's neuromorphic response.

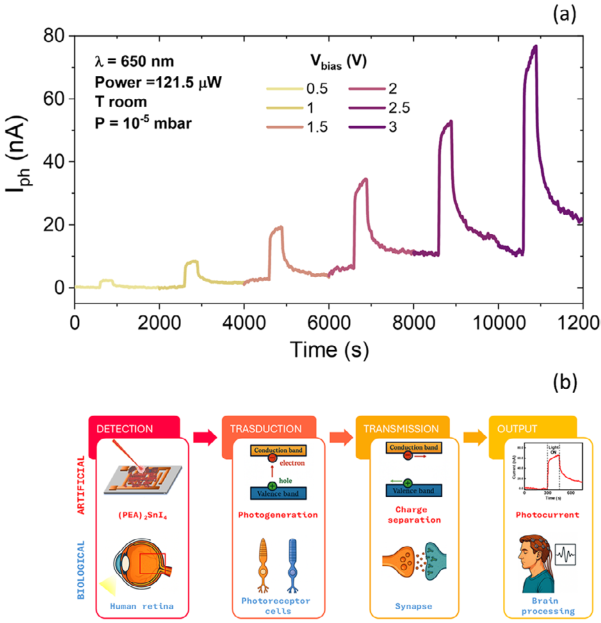

Figure 5. a) Photocurrent response to a train of light pulses (duration = 100 s, P = 121.5 μW) with increasing polarisation voltages from 0.5 to 3 V. The signal shows cumulative growth and prolonged decay, characteristic of short-term synaptic plasticity. b) Conceptual schematic illustration of the neuromorphic behaviour of photoreceptors $(PEA)_2SnI_4$. The diagram shows an analogy with the biological retina-synapse-brain pathway, in which the artificial system (top row) mimics the biological pathway (bottom row) from light detection to signal output. In both cases, the process involves detection (retina or photodetector), transduction (photogeneration of charge carriers or activation of photoreceptors), transmission (charge separation or synaptic signaling), and output (photocurrent generation or brain processing).

3.3. Temperature Dependence of PEA_2SnI_4 Conductivity

Finally, we investigate the effect of the temperature on the conductivity of PEA_2SnI_4. **Figure 6a** reports the IV curves under dark conditions as a function of the temperature ranging from 100 to 275 K. An increase in dark current with temperature is observed up to 225 K, after which the current decreases with increasing temperature. A more detailed study of this behavior is shown in Figure 6b. The current (blue shaded squares), measured at V_{ds} = 0.5 V, increases significantly up to 225 K, indicating thermal excitation to the conduction band. At higher temperatures (225–275 K), a noticeable change in the current trend appears. This suggests that phonon scattering or other mechanisms, such as ion migration, begin to play a role in charge transport, provided a structural phase transition can be excluded. To rule out this possibility, we performed single-crystal XRD (SC-XRD) analysis at 180, 220 and 273K. As detailed in Table S1 (Supporting Information), $(PEA)_2SnI_4$ single crystal adopts a triclinic P1

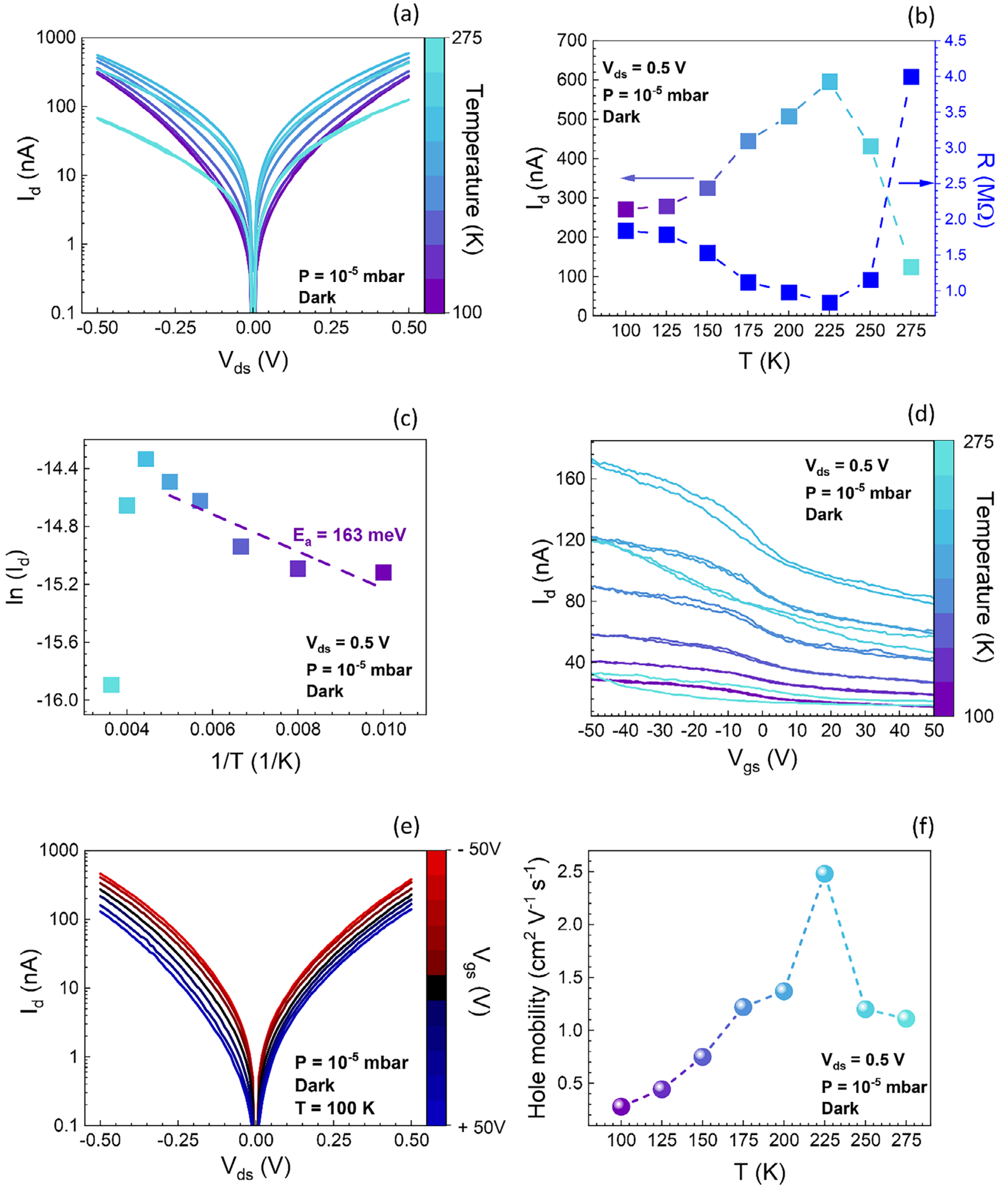

Figure 6. a) *I–V* in dark condition at different temperatures. b) Current and resistance as a function of temperature at V = 0.5 V. c) Arrhenius plot of the current vs 1/T. d) Transfer curves at different temperatures. e) Output at a temperature of 100 K. f) Hole mobility vs temperature. All measurements are performed at a pressure of 10^{-5} mbar.

structure, in agreement with single-crystal determinations previously reported for this material.[69] Across 180–273 K, the lattice parameters evolve smoothly with temperature and show no discontinuities. The unit-cell volume increases monotonically from 1216 to 1227 Å^3. Thermal expansion is anisotropic and most pronounced along c, in the direction perpendicular to the inorganic conductive layers, as expected for a layered ($n = 1$) structure. Overall, the data indicate a thermally driven, anisotropic expansion without evidence of a structural phase transition in the investigated range.

The possible formation of a space charge region could explain the deviation from purely thermally activated transport. In Figure 6c, we report the temperature-dependent I_d, plotted in Arrhenius form, allowing the extraction of the activation energy, E_a, according to:

$$\ln\left(I_d\right) = A - \frac{E_a}{k_B T} \tag{3}$$

where A is a constant, k_B is Boltzmann's constant, and T is absolute temperature.[31] In the low-temperature range (100–225 K), the data follow a clear linear trend (see dashed violet curve) with an activation energy of 163 meV, consistent with thermally activated transport limited by shallow traps. At high temperatures (225–275 K), the Arrhenius behavior deviates from linearity, indicating that thermally activated conduction is no longer the dominant transport mechanism. This trend, also shown by the resistance profile shown in Figure 6b (see blue squares), marks a crossover to a regime primarily governed by phonon-limited mobility.[31]

Additionally, thermally activated ionic species (e.g., Sn vacancies or halide ions) may also migrate under bias and accumulate near the contacts, partially screening the electric field and further reducing the electronic current.[19] Figure 6d shows the transfer characteristic of the device at a drain voltage, $\mathrm{V_{ds}}$, of 0.5 V, and a gate voltage ($\mathrm{V_{gs}}$) ranging from −50 to 50 V for different temperatures (100 – 275 K). We observe an increase in drain current by increasing the temperature up to 225 K and a p-type self-doping behavior due to the oxidation of $\mathrm{Sn^{2+}}$ to $\mathrm{Sn^{4+}}$ and the low formation energy of Sn vacancies, which contributes a hole-dominated photocurrent.[17,20] As the temperature is raised above 225 K, the gate field effect becomes increasingly ineffective, likely due to the activation of ion migration, which causes the screening of the gate electric field, in agreement with other studies on $\mathrm{MAPbI_3}$ transistors.[31] This confirms a temperature threshold for ion migration above 225 K. The output characteristics (Figure 6e), at the lowest temperature of 100 K, further validate the p-type behaviour. Figure 6f presents the maximum field effect mobility of the perovskite as a function of temperature at 10^{-5} mbar under dark conditions. To quantify the hole mobility, μ_h, we apply the standard FET formula for the linear region of the transfer curve[70]:

$$\mu_h = \frac{L}{5\ W\ C_{ox} V_{ds}} \left|\frac{dI_d}{dV_{gs}}\right|_{max} \tag{4}$$

where $L = 1200\ \mu m$ and $W = 37.5\ \mu m$ are the channel length and width, respectively, $C_{ox}\ =\ 1.15 \times\ 10^{-8}\ F\ cm^{-2}$ is the oxide capacitance of $\mathrm{SiO_2}$, and dI_d/dV_{gs} is the transconductance in the on-state. 5 is the number of channels in parallel. At low temperatures (100–175 K), μ_h rises gradually from ≈0.2 to 1 cm^2 V^{-1} s^{-1}. The charge transport is dominated by holes moving through shallow trap states, with negligible phonon diffusion and no detectable ionic movement. In the intermediate range (175–225 K), μ_h increases more steeply and reaches a maximum of ≈2.5 cm^2 V^{-1} s^{-1} at 225 K. In this case, carriers acquire sufficient thermal energy to overcome the trap barriers more efficiently, then the current follows a thermally activated regime and mobility reaches its maximum (Figure 6f). Above 225 K, μ_h decreases to ≈1 cm^2 V^{-1} s^{-1} as temperature approaches 275 K, a trend typical of phonon-limited mobility. In this high-temperature window, mobile ionic defects (e.g., Sn vacancies or halide ions) can migrate over short distances and partially shield the internal electric field, contributing to the hysteresis observed in the transfer curves (Figure 6d). As a result, charge transport remains dominated by holes, but is modulated by phonon diffusion and field shielding effects at higher temperatures. These observations indicate a transition from low-temperature trap-controlled transport to band-like conduction with a mobility peak around 225 K, followed by transport limited by phonon diffusion at higher temperatures, consistent with the conductivity reversal in Figure 6b.

4. Conclusion

In this work, we systematically studied photoluminescence (PL) and photoconductivity of 2D lead-free perovskite $\mathrm{PEA_2SnI_4}$. Environmental stability investigations revealed a surface degradation upon air exposure, characterized by an initial rapid PL decay followed by partial stabilization in the dark. Under continuous illumination, accelerated degradation was observed, confirming the role of light-induced instabilities. Importantly, the total recovery of PL intensity after exfoliation suggested that bulk $\mathrm{PEA_2SnI_4}$ remains intact, highlighting opportunities for performance restoration through surface engineering. Moreover, the optoelectronic investigation of a $\mathrm{PEA_2SnI_4}$ interdigitated photodetector exhibited a photoresponsivity of ≈ 60 A W^{-1} under low-intensity 650 nm and sublinear power dependence ($\alpha = 0.33$), indicative of trap-assisted conduction and space charge effects. Bias-dependent measurements confirmed device operation in the space charge-limited current (SCLC) regime, with a quadratic I–V behavior. Time-resolved photocurrent analysis revealed the coexistence of fast and slow relaxation components, modulated by the applied bias, consistent with the mechanisms of carrier trapping, space charge accumulation, and ion redistribution. Notably, persistent photocurrent and double-exponential decay dynamics emulate the characteristics of short-term synaptic plasticity in neuromorphic systems. The observed cumulative response to optical stimuli suggests that $\mathrm{PEA_2SnI_4}$ photodetectors may act as artificial synapses, suitable for bioinspired photonic computation, adaptive learning systems, and visual signal preprocessing. Temperature-dependent transport studies revealed a transition from thermally activated conduction to mobility degradation by phonon scattering above 225 K, with a maximum mobility of 2.5 cm^2 V^{-1} s^{-1}. Overall, our results confirm $\mathrm{PEA_2SnI_4}$ as a promising lead-free perovskite material for low-power optoelectronics and adaptive neuromorphic systems, while emphasizing the need for surface passivation strategies to ensure long-term environmental stability.

5. Experimental Section

Synthesis: A precursor solution of PEA$_2$SnI$_4$ 1.8 M in γ-butyrolactone (GBL) was prepared by dissolving tin iodide (SnI$_2$) (from Sigma–Aldrich) and phenethylammonium iodide (PEAI) (from Greatcellsolar) in a 1:2 molar ratio and maintaining the mixture in a hot plate at 70 °C under continuous stirring for 12 h. The solution was filtered before use. Single-crystal PEA$_2$SnI$_4$ was grown by utilizing the space-confined method. Prior to growth, quartz substrates measuring 1.5 cm × 1.5 cm were cleaned via sonication in acetone, followed by rinsing in isopropyl alcohol. Inside a nitrogen atmosphere glovebox, the substrates were then stacked slightly shifted from one another and thermalized for 5 min in the oven at a temperature of 80 °C to avoid thermal shock. 10 µL of the precursor solution was then infiltrated in the space between the substrates by depositing the droplet at the border of the upper substrate. The samples were then kept in a nitrogen-filled container and transferred to an oven, where the samples were grown in a vacuum using a scroll pump. Inside the oven, the temperature was slowly ramped down from 80 to 20 °C at a rate of 1.5 °C h^{-1}.

X-Ray Diffraction: The X-ray diffraction patterns of the films were obtained with a Bruker D8 Advance X-ray diffractometer employing a Cu Ka radiation (40 kV/40 mA) and a Goebel mirror in a theta/2theta geometry and recorded with a 0.025° step size and 0.5 s per step. Temperature-dependent Single-crystal X-ray diffraction data were collected on a Bruker D8 Venture diffractometer equipped with a high-brilliance microfocus MoKα source, a PHOTON-II detector (C-PAD technology), and an Oxford CryoSystem 800 cryostat operating over the temperature range 298–100 K.

Atomic Force Microscopy: AFM images have been acquired with a Horiba AINST-NT AFM, using the non-contact mode technique. All raw data have been analyzed by using the *WSxM* 5.0 software by NanoTec, 2015.

Optical Characterization: The optical absorption was measured using a Jasco V-770 UV–vis spectrophotometer. The steady-state photoluminescence spectrum of the crystals was acquired by using a custom-made setup, by optically exciting the sample with an LED with a wavelength of 405 nm and a power of 1 mW.

Device Fabrication: Ti/Au (5/60 nm) interdigitated metal electrodes were pre-patterned on Si^{++}/SiO$_2$ (280 µm/300 nm) substrates, using direct laser writing optical lithography followed by metal thermal evaporation. The device channel length was 7 µm. Single crystal flakes were then transferred using a Nitto ELP BT-150E-KL tape on the pre-patterned devices and stored in a vacuum for 1 month before use.

Electrical Characterization: Electrical measurements were performed utilizing a Janis ST-500 cryogenic probe station coupled to a Keithley 4200 SCS semiconductor characterization system, having a sensitivity to current and voltage of ≈0.1 pA and 2 µV, respectively.

Supporting Information

Supporting Information is available from the Wiley Online Library or from the author.

Acknowledgements

V.D. acknowledges the support of the Project ′Network 4 Energy Sustainable Transition—NEST′, Spoke 1, Project code PE0000021, funded under the National Recovery and Resilience Plan (NRRP), Mission 4, Component 2, Investment 1.3— Call for tender No. 1561 of 11.10.2022 of Ministero dell'Università e della Ricerca (MUR); funded by the European Union—NextGenerationEU. V.D. and M.S. acknowledge Ecosystem of Innovation for Next Generation Sardinia, Spoke 7-Project code ECS00000038 (Low carbon technologies for efficient energy system). G.B., A.M., D.M. acknowledge the support of the Projects 2022XP37CA-Newatomists and PRIN 2022 PNRR grant P20224PJJN-Orienting. D.M. acknowledges the MUR fund through PRIN 2022 grants: 2022EHER2H-ISoTOPe. A.D.B. and O.D. acknowledge the financial support from the University of Salerno, with grants ORSA223384 and ORSA235199. H.T.L, K.J.R, M.F.C. and S.R. acknowledge financial support from the Leverhulme Trust (grants "Graded excitonics" and "Giant Permittivity"), EPSRC (Grant no. EP/K010050/1, EP/M001024/1, EP/M002438/1, EP/Z534250/1, EP/Y021339/1, EPSRC Core Equipment 2024-UKRI323), EU H2020-MSCA-RISE projects TERASSE (Project No. 823878) and CHARTIST (Project No. 101007896), and the EU MSCA Staff Exchanges project HERMES (Project No. 101236439), and the Royal Society International Fellowship Kang Tong Po and International Exchanges IES\R2\252147. F. P. acknowledges partial financial support under the National Recovery and Resilience Plan (NRRP), Mission 4, Component 2, Investment 1.1, Call PRIN 2022 by the Italian Ministry of University and Research (MUR), funded by the European Union – NextGenerationEU – EQUATE Project, "Defect engineered graphene for electro-thermal quantum technology" - Grant Assignment Decree No. 2022Z7RHRS. F.P. acknowledges partial financial support under Scientific Committee V of the National Institute for Nuclear Physics (INFN) under the Technology Innovation Grant 2025 - STEEP Project. All authors acknowledge CeSAR-Centro Servizi di Ateneo per la Ricerca-at the Università degli Studi di Cagliari (Dr. E. Podda for technical assistance on XRD).

Conflict of Interest

The authors declare no conflict of interest.

Author Contributions

O.D. and V.D. shared authorship.

Data Availability Statement

The data that support the findings of this study are available from the corresponding author upon reasonable request.

Keywords

2D Hybrid Perovskite, artificial synapses, lead-free single-crystals PEA2SnI4, neuromorphic applications, space charge limited current (SCLC)

Received: October 9, 2025
Revised: November 19, 2025
Published online:

---

[1] V. Demontis, O. Durante, D. Marongiu, S. De Stefano, S. Matta, A. Simbula, C. Ragazzo Capello, G. Pennelli, F. Quochi, M. Saba, A. Di Bartolomeo, A. Mura, G. Bongiovanni, *Adv. Opt. Mater.* **2024**, *13*, 2402469.
[2] R. Mastria, K. J. Riisnaes, A. Bacon, I. Leontis, H. T. Lam, M. A. S. Alshehri, D. Colridge, T. H. E. Chan, A. De Sanctis, L. De Marco, L. Polimeno, A. Coriolano, A. Moliterni, V. Olieric, C. Giannini, S. Hepplestone, M. F. Craciun, S. Russo, *Adv. Funct. Mater.* **2024**, *34*, 2401903.
[3] K. J. Riisnaes, M. Alshehri, I. Leontis, R. Mastria, H. T. Lam, L. De Marco, A. Coriolano, M. F. Craciun, S. Russo, *ACS Appl. Mater. Interfaces* **2024**, *16*, 31399.
[4] C.-H. Liao, M. A. Mahmud, A. W. Y. Ho-Baillie, *Nanoscale* **2023**, *15*, 4219.
[5] X. Liu, D. Yu, X. Song, H. Zeng, *Small* **2018**, *14*, 1801460.
[6] A. Liu, H. Zhu, S. Bai, Y. Reo, M. Caironi, A. Petrozza, L. Dou, Y.-Y. Noh, *Nat. Electron.* **2023**, *6*, 559.

[7] Y. Xi, G. Li, T. Ji, Y. Hao, S. F. Liu, Y. Liu, Y. Cui, *Adv. Funct. Mater.* **2024**, *34*, 2407525.

[8] J. Wang, Y. Che, Y. Duan, Z. Liu, S. Yang, D. Xu, Z. Fang, X. Lei, Y. Li, S. F. Liu, *Adv. Mater.* **2023**, *35*, 2210223.

[9] J. Jeong, M. Kim, J. Seo, H. Lu, P. Ahlawat, A. Mishra, Y. Yang, M. A. Hope, F. T. Eickemeyer, M. Kim, Y. J. Yoon, I. W. Choi, B. P. Darwich, S. J. Choi, Y. Jo, J. H. Lee, B. Walker, S. M. Zakeeruddin, L. Emsley, U. Rothlisberger, A. Hagfeldt, D. S. Kim, M. Grätzel, J. Y. Kim, *Nature* **2021**, *592*, 381.

[10] S. Ullah, J. Wang, P. Yang, L. Liu, S.-E. Yang, T. Xia, H. Guo, Y. Chen, *Mater. Adv.* **2021**, *2*, 646.

[11] M. I. Saidaminov, M. A. Haque, J. Almutlaq, S. Sarmah, X. Miao, R. Begum, A. A. Zhumekenov, I. Dursun, N. Cho, B. Murali, O. F. Mohammed, T. Wu, O. M. Bakr, *Adv. Opt. Mater.* **2017**, *5*, 1600704.

[12] M. S. Collin, S. K. Venkatraman, N. Vijayakumar, V. Kanimozhi, S. M. Arbaaz, R. G. S. Stacey, J. Anusha, R. Choudhary, V. Lvov, G. I. Tovar, F. Senatov, S. Koppala, S. Swamiappan, *J. Hazard. Mater. Adv.* **2022**, *7*, 100094.

[13] L. Check, A. Marteel-Parrish, *Rev. Environ. Health* **2013**, *28*, 85.

[14] G. I. Edo, P. O. Samuel, G. O. Oloni, G. O. Ezekiel, V. O. Ikpekoro, P. Obasohan, J. Ongulu, C. F. Otunuya, A. R. Opiti, R. S. Ajakaye, A. E. A. Essaghah, J. J. Agbo, *Chem. Ecol.* **2024**, *40*, 322.

[15] R. Kour, S. Arya, S. Verma, J. Gupta, P. Bandhoria, V. Bharti, R. Datt, V. Gupta, *Glob. Chall.* **2019**, *3*, 1900050.

[16] M. He, Z. Xu, C. Zhao, Y. Gao, K. Ke, N. Liu, X. Yao, F. Kang, Y. Shen, L. Lin, G. Wei, *Adv. Funct. Mater.* **2023**, *33*, 2300282.

[17] L. Qian, Y. Sun, M. Sun, Z. Fang, L. Li, D. Xie, C. Li, L. Ding, *J. Mater. Chem. C* **2019**, *7*, 5353.

[18] L. Qian, Y. Sun, M. Wu, C. Li, D. Xie, L. Ding, G. Shi, *Nanoscale* **2018**, *10*, 6837.

[19] S. Yang, J. Wen, Y. Wu, H. Zhu, A. Liu, Y. Hu, Y. Noh, J. Chu, W. Li, *Small* **2024**, *20*, 2304626.

[20] K. J. Savill, A. M. Ulatowski, L. M. Herz, *ACS Energy Lett.* **2021**, *6*, 2413.

[21] W. Yang, L. Dou, H. Zhu, Y. Noh, *Small Struct.* **2024**, *5*, 2300393.

[22] S. Sen, S. Gopalan, R. Sellappan, A. N. Grace, P. Sonar, *Adv. Energy Sustain. Res.* **2023**, *4*, 2300110.

[23] D. Ju, X. Jiang, H. Xiao, X. Chen, X. Hu, X. Tao, *J. Mater. Chem. A* **2018**, *6*, 20753.

[24] E. Foadian, J. Yang, Y. Tang, S. B. Harris, C. M. Rouleau, S. Joy, K. R. Graham, B. J. Lawrie, B. Hu, M. Ahmadi, *Adv. Funct. Mater.* **2023**, *34*, 2411164.

[25] I. Chao, Y. Yang, M. Yu, C. Chen, C. Liao, B. Lin, I. Ni, W. Chen, A. W. Y. Ho-Baillie, C. Chueh, *Small* **2023**, *19*, 2207734.

[26] Y. Ju, X. Wu, S. Huang, G. Dai, T. Song, H. Zhong, *Adv. Funct. Mater.* **2022**, *32*, 2108296.

[27] C. Chen, M. Yu, Y. Wang, Y. Tseng, I. Chao, I. Ni, B. Lin, Y. Lu, C. Chueh, *Small* **2024**, *20*, 2307774.

[28] K. Wang, C. Wu, D. Yang, Y. Jiang, S. Priya, *ACS Nano* **2018**, *12*, 4919.

[29] N. Wang, L. Cheng, R. Ge, S. Zhang, Y. Miao, W. Zou, C. Yi, Y. Sun, Y. Cao, R. Yang, Y. Wei, Q. Guo, Y. Ke, M. Yu, Y. Jin, Y. Liu, Q. Ding, D. Di, L. Yang, G. Xing, H. Tian, C. Jin, F. Gao, R. H. Friend, J. Wang, W. Huang, *Nat. Photon.* **2016**, *10*, 699.

[30] L.-Y. Ma, N. Soin, S. N. Aidit, F. A. Md Rezali, S. F. Wan, M. Hatta, *Mater. Sci. Semicond. Process.* **2023**, *165*, 107658.

[31] C. Huo, X. Liu, X. Song, Z. Wang, H. Zeng, *J. Phys. Chem. Lett.* **2017**, *8*, 4785.

[32] A. Bhardwaj, D. Marongiu, V. Demontis, A. Simbula, F. Quochi, M. Saba, A. Mura, G. Bongiovanni, *Nanomaterials* **2024**, *14*, 1444.

[33] Q. Liu, Y. Yuan, J. Liu, W. Wang, J. Chen, W. Xu, *Mater. Today Electron.* **2024**, *8*, 100099.

[34] D. Li, X. Dong, P. Cheng, L. Song, Z. Wu, Y. Chen, W. Huang, *Adv. Sci.* **2022**, *9*, 2203683.

[35] A. Younis, C. Lin, X. Guan, S. Shahrokhi, C. Huang, Y. Wang, T. He, S. Singh, L. Hu, J. R. D. Retamal, J. He, T. Wu, *Adv. Mater.* **2021**, *33*, 2005000.

[36] J. Choi, J. S. Han, K. Hong, S. Y. Kim, H. W. Jang, *Adv. Mater.* **2018**, *30*, 1704002.

[37] C. Chen, X. Zhang, G. Wu, H. Li, H. Chen, *Adv. Opt. Mater.* **2017**, *5*, 1600539.

[38] Y. Chen, Y. Sun, J. Peng, J. Tang, K. Zheng, Z. Liang, *Adv. Mater.* **2018**, *30*, 1703487.

[39] M. A. Haque, J. Troughton, D. Baran, *Adv. Energy Mater.* **2020**, *10*, 1902762.

[40] J. Wan, H. Yuan, Z. Xiao, J. Sun, Y. Peng, D. Zhang, X. Yuan, J. Zhang, Z. Li, G. Dai, J. Yang, *Small* **2023**, *19*, 2207185.

[41] J. Kim, W. Lee, K. Cho, H. Ahn, J. Lee, K.-Y. Baek, J.-K. Kim, K. Kang, T. Lee, *Nanotechnology* **2021**, *32*, 185203.

[42] M. I. Saidaminov, A. L. Abdelhady, B. Murali, E. Alarousu, V. M. Burlakov, W. Peng, I. Dursun, L. Wang, Y. He, G. Maculan, A. Goriely, T. Wu, O. F. Mohammed, O. M. Bakr, *Nat. Commun.* **2015**, *6*, 7586.

[43] A. Simbula, V. Demontis, F. Quochi, G. Bongiovanni, D. Marongiu, *ACS Omega* **2024**, *9*, 36865.

[44] V. D. Mihailetchi, J. Wildeman, P. W. M. Blom, *Phys. Rev. Lett.* **2005**, *94*, 126602.

[45] R. H. Bube, *J. Appl. Phys.* **1962**, *33*, 1733.

[46] E. A. Duijnstee, J. M. Ball, V. M. Le Corre, L. J. A. Koster, H. J. Snaith, J. Lim, *ACS Energy Lett.* **2020**, *5*, 376.

[47] V. M. Le Corre, E. A. Duijnstee, O. El Tambouli, J. M. Ball, H. J. Snaith, J. Lim, L. J. A. Koster, *ACS Energy Lett.* **2021**, *6*, 1087.

[48] I. Suárez, J. Sánchez-Díaz, H. Pashaei Adl, I. Mora-Seró, J. P. Martínez-Pastor, *Adv. Optic. Mater.* **2025**, *13*, 2402372.

[49] A. Sembito, M. M. Ligavo, J. M. Mwabora, F. W. Nyongesa, M. Diale, *Vacuum* **2025**, *233*, 113954.

[50] W. Shuanglong, PhD Thesis, Johannes Gutenberg Universitat Mainz, Mainz, Germany, **2023**.

[51] S. Cai, Y. Ju, Y. Wang, X. Li, T. Guo, H. Zhong, L. Huang, *Adv. Sci.* **2022**, *9*, 2104708.

[52] X. Ma, H. Gao, C. Meng, F. Pan, H. Ye, *J. Phys. Chem. Lett.* **2023**, *14*, 6860.

[53] D. Ricciarelli, D. Meggiolaro, F. Ambrosio, F. De Angelis, *ACS Energy Lett.* **2020**, *5*, 2787.

[54] S. M. SZE, M.-K. LEE, in *Semiconductor Devices: Physics and Tecnology*, *4*, John Wiley & Sons, Hoboken, NJ, USA, **2021**.

[55] Y. Zhang, Y. Ma, Y. Wang, X. Zhang, C. Zuo, L. Shen, L. Ding, *Adv. Mater.* **2021**, *33*, 2006691.

[56] B. T. Van Gorkom, T. P. A. Van Der Pol, K. Datta, M. M. Wienk, R. A. J. Janssen, *Nat. Commun.* **2022**, *13*, 349.

[57] B. T. Van Gorkom, A. Simons, W. H. M. Remmerswaal, M. M. Wienk, R. A. J. Janssen, *ACS Appl. Energy Mater.* **2024**, *7*, 5869.

[58] E. Choi, Y. Zhang, A. M. Soufiani, M. Lee, R. F. Webster, M. E. Pollard, P. J. Reece, W. Lee, J. Seidel, J. Lim, J.-H. Yun, J. S. Yun, *npj 2D Mater. Appl.* **2022**, *6*, 43.

[59] A. Simbula, L. Wu, F. Pitzalis, R. Pau, S. Lai, F. Liu, S. Matta, D. Marongiu, F. Quochi, M. Saba, A. Mura, G. Bongiovanni, *Nat. Commun.* **2023**, *14*, 4125.

[60] H. Xue, Z. Chen, S. Tao, G. Brocks, *ACS Energy Lett.* **2024**, *9*, 2343.

[61] K. Domanski, W. Tress, T. Moehl, M. Saliba, M. K. Nazeeruddin, M. Grätzel, *Adv. Funct. Mater.* **2015**, *25*, 6936.

[62] R. Xiao, Y. Hou, Y. Fu, X. Peng, Q. Wang, E. Gonzalez, S. Jin, D. Yu, *Nano Lett.* **2016**, *16*, 7710.

[63] P. C. Y. Chow, N. Matsuhisa, P. Zalar, M. Koizumi, T. Yokota, T. Someya, *Nat. Commun.* **2018**, *9*, 4546.

[64] A. Rose, *Phys. Rev.* **1955**, *97*, 1538.

[65] A. Kumar, K. Intonti, L. Viscardi, O. Durante, A. Pelella, O. Kharsah, S. Sleziona, F. Giubileo, N. Martucciello, P. Ciambelli, M. Schleberger, A. Di Bartolomeo, *Mater. Horiz.* **2024**, *11*, 2397.

[66] G. Vats, B. Hodges, A. J. Ferguson, L. M. Wheeler, J. L. Blackburn, *Adv. Mater.* **2023**, *35*, 2205459.

[67] D. Hao, Z. Yang, J. Huang, F. Shan, *Adv. Funct. Mater.* **2023**, *33*, 2211467.

[68] J. Xia, Z. Wan, C. Peng, Y. Liu, P.-A. Chen, H. Wei, J. Ding, Y. Zhang, Y. Hu, *ACS Appl. Mater. Interfaces* **2025**, *17*, 10886.

[69] Y. Gao, Z. Wei, P. Yoo, E. Shi, M. Zeller, C. Zhu, P. Liao, L. Dou, *J. Am. Chem. Soc.* **2019**, *141*, 15577.

[70] T. Wu, W. Pisula, M. Y. A. Rashid, P. Gao, *Adv. Electron. Mater.* **2019**, *5*, 1900444.